

Dislocation-mediated short-range order evolution during thermomechanical processing

Mahmudul Islam¹, Killian Sheriff¹, and Rodrigo Freitas^{1*}

¹*Department of Materials Science and Engineering, Massachusetts Institute of Technology, Cambridge, MA, USA*

Abstract

Thermomechanical processing alters the microstructure of metallic alloys through coupled plastic deformation and thermal exposure, with dislocation motion driving plasticity and microstructural evolution. Our previous work¹ showed that the same dislocation motion both creates and destroys chemical short-range order (SRO), driving alloys into far-from-equilibrium SRO states. However, the connection between this dislocation-mediated SRO evolution and processing parameters remains largely unexplored. Here, we perform large-scale atomistic simulations of thermomechanical processing of equiatomic TiTaVW to determine how temperature and strain rate control SRO via competing creation (Γ) and annihilation (λ) rates. Using machine learning interatomic potentials and information-theoretic metrics, we quantify that the magnitude and chemical character of SRO vary systematically with these parameters. We identify two regimes: a low-temperature regime with weak strain-rate sensitivity, and a high-temperature regime in which reduced dislocation density and increased screw character amplify chemical bias and accelerate SRO formation. The resulting steady-state SRO is far-from-equilibrium and cannot be produced by equilibrium thermal annealing. Together, these results provide a mechanistic and predictive link between processing parameters, dislocation physics, and SRO evolution in chemically complex alloys.

1. Introduction

Thermomechanical processing (TMP) is a widely employed manufacturing technique in which alloys are strained at controlled temperatures to induce microstructural evolution via plastic deformation^{2–7}. Plastic deformation is most often governed by dislocation motion; therefore, the mechanical response of a material undergoing TMP reflects dislocation behavior. That behavior is controlled by temperature and strain rate — the two primary parameters of TMP^{8–10}. For example, at low temperatures, dislocation motion is primarily governed by the Peierls barrier, whereas at high temperatures dislocations become thermally activated and can overcome this barrier more readily, reducing the flow stress at a fixed strain rate¹¹. Furthermore, increasing temperature activates qualitatively different modes of dislocation motion such as diffusion-assisted climb, and cross-slip — which are largely suppressed at low temperatures¹². High strain rates, on the other hand, raise the flow stress so that dislocations surmount Peierls barriers with reduced thermal assistance (i.e., athermal glide). Increasing strain rate also promotes dislocation multiplication in order to sustain the high rate of plastic deformation¹³. This leads to the formation of dense dislocation forests and junctions, many of which are sessile, that hinder the motion of glissile dislocations, resulting in strain hardening.

Fundamentally, dislocation motion is a bond-breaking and bond-forming process that alters the local chemical environment in the wake of moving dislocation cores. A large number of dislocations traversing through the system can thus modify the relative population of certain local chemical motifs, thereby altering spatial chemical correlations at the nanoscale — commonly referred to as chemical short-range order (SRO)^{14–16}. SRO has been reported to influence several materials properties, including mechani-

cal strength^{17–21}, radiation damage resistance^{22,23}, catalysis²⁴, and corrosion resistance^{25–27}, especially in alloys with pronounced chemical complexity, such as high-entropy alloys²⁸. In ref. 1, we demonstrated that dislocation motion both creates and destroys SRO, driving alloys into far-from-equilibrium SRO states. Notably, even alloys initialized as chemically random solid solutions evolve SRO under plastic deformation. The mechanism underlying this phenomenon was attributed to the chemically biased nature of dislocation motion in alloys, which promotes certain motifs over others^{29–31}. As described earlier, dislocation behavior is strongly dependent on temperature and strain rate. Consequently, a natural correlation must exist between these TMP parameters and the evolution of SRO via dislocation motion. However, this relationship remains obscure in the literature, leaving a critical gap in our understanding of how SRO evolves in metallic alloys. Without a mechanistic understanding of how dislocation motion affects SRO under different TMP conditions, interpretations of deformation experiments risk conflating intrinsic mechanical response with concurrent changes in SRO, and models cannot reliably predict regimes where nonequilibrium SRO dominates. This gap limits transferability across alloys and invites equilibrium-based extrapolations^{32–34} that are systematically misleading for TMP.

Here, we investigate the effects of temperature and strain rate on the evolution of SRO in equiatomic TiTaVW alloy during TMP using large-scale atomistic simulations. These simulations — performed on the Frontier exascale supercomputer³⁵ — employ a high-fidelity machine learning interatomic potential that was trained on ab initio data tailored to capture the structure and chemistry relevant to TMP (section 2.1). We select equiatomic TiTaVW as a canonical refractory alloy with a high Peierls barrier and screw-dominated plasticity, providing a stringent testbed for chemically-biased dislocation motion. In sections 3.1–

*Corresponding author (rodrigof@mit.edu).

3.3 we demonstrate how TMP processing parameters influence SRO evolution. The dislocation motion mechanisms underlying SRO evolution are discussed in section 3.4. Finally, in section 3.5, we implement an empirical model based on our simulations results to explore steady-state SRO under conditions relevant to practical manufacturing processes.

2. Methods

2.1. Machine learning interatomic potential

To conduct accurate atomistic simulations of equiatomic TiTaVW alloy, we developed a machine learning interatomic potential tailored to capture the chemistry-sensitive mechanisms governing dislocation behavior under thermo-mechanical loading — mechanisms that conventional empirical potentials fail to represent accurately^{14,36}. The training dataset for the potential included both perfect and defect configurations, carefully curated to capture the chemical and structural complexity relevant to the TMP of TiTaVW alloy. The perfect configurations included body-centered cubic (bcc), face-centered cubic (fcc), and hexagonal close-packed (hcp) solid solutions, pure elemental bcc structures, and B2 structures representing all binary combinations. The fcc and hcp phases were included to account for phase stability, with fcc supercells specifically added due to their demonstrated ability to accurately capture screw dislocation core characteristics^{37,38}.

Defect configurations were chosen based on well-established mechanisms governing plastic deformation in bcc systems, which is primarily mediated by the motion of $\frac{1}{2}\langle 111 \rangle$ screw dislocations. The properties of these dislocations are strongly influenced by the stacking-fault energy (SFE) landscapes on the (110) and (112) planes^{39,40}. Accordingly, we included configurations with stacking faults along the [111] direction on these planes. However, SFE curves alone are insufficient to fully represent the highly anisotropic core structures of dislocations in bcc systems⁴¹. To address this, we incorporated configurations containing $\frac{1}{2}\langle 111 \rangle\{110\}$ screw dislocations generated via the dislocation dipole method⁴², as well as configurations with $\frac{1}{2}\langle 111 \rangle\{110\}$ edge dislocation dipoles for their relevance in bcc plasticity⁴³. Finally, we included bcc configurations with both vacancies and interstitials (placed at either tetrahedral or octahedral sites) to account for defect-mediated mechanisms relevant to dislocation motion.

For all solid-solution phases, elemental compositions were sampled across the full TiTaVW local motif space using the motif-based algorithm of ref. 44. To bias the training dataset toward near equiatomic compositions, the procedure was adapted by first generating a diverse set of chemically random solutions and then allowing extra-cell swaps between configurations. This allowed greater flexibility to increase motif diversity, especially in low-data regimes, while favoring near equiatomic configurations to be represented.

The lattice constants of these structures were adjusted using Vegard’s law to the sampled compositions. To mimic

thermal vibrations, atomic displacements were applied by randomly perturbing atoms following the methodology in ref. 44. Isotropic lattice expansion was further applied to imitate both room-temperature and high-temperature thermal expansion³⁶.

Density functional theory (DFT) calculations were performed to obtain energies and atomic forces for all configurations in the dataset. These calculations used the Perdew-Burke-Ernzerhof (PBE) exchange-correlation functional⁴⁵ and projector-augmented wave (PAW) pseudopotentials⁴⁶, as implemented in VASP^{47–51}. The resulting DFT energies and forces were used to train a machine learning interatomic potential based on the atomic cluster expansion framework, with hyperparameter optimized to balance both accuracy and generalization^{44,52,53}.

All molecular dynamics and Monte Carlo simulations reported here were conducted using the developed machine learning interatomic potential.

2.2. Thermomechanical processing simulations

The central simulations underpinning the results of this paper were molecular dynamics simulations of uniaxial compressive deformation on bcc single crystals of TiTaVW alloy using the Large-scale Atomic/Molecular Massively Parallel Simulator (LAMMPS)⁵⁴. Simulation cells were initialized by randomly populating bcc lattice sites with Ti, Ta, V, and W atoms in equiatomic proportions. The initial simulation box measured $53a_o \times 106a_o \times 212a_o$ along the [100], [010], and [001] directions, respectively, where a_o is the temperature-dependent lattice constant. Each configuration contained approximately 2.4 million atoms, with periodic boundary conditions applied in all directions.

To introduce initial plasticity carriers, four hexagonal, vacancy-type prismatic dislocation loops with a diameter of 10 nm were embedded in the system. Each loop was assigned one of the four Burgers vectors of type $\frac{1}{2}\langle 111 \rangle$, resulting in an initial dislocation density of $3.6 \times 10^{15} \text{ m}^{-2}$. The loops were placed randomly while avoiding overlaps, as illustrated in fig. 1a.

The dislocation-seeded structures were first equilibrated at constant temperatures T ranging from 300 K to 2,300 K and zero pressure using a Nosé-Hoover thermostat and a Nosé-Hoover barostat, respectively, for 100 ps, allowing isotropic volume relaxation. After equilibration, mechanical deformation^{55,56} was applied in compression along the [001] axis at constant strain rates $\dot{\epsilon}$ ranging from 10^8 s^{-1} to 10^9 s^{-1} , while maintaining zero lateral pressure via the Nosé-Hoover barostat in the [100] and [010] directions. Temperature, which remained the same as the equilibration temperature, was controlled using a Nosé-Hoover thermostat throughout deformation. For all thermostats and barostats applied throughout the simulations, we used a damping parameter of 10 ps and a chain length of 3.

After every unit strain, the compression axis was rotated sequentially from [001] to $[0\bar{1}0]$, then to [100], and again back to [001]. This procedure was repeated until a total true strain of 7 was reached. This cyclic deformation process (the first three cycles of which are illustrated in fig. 1a)

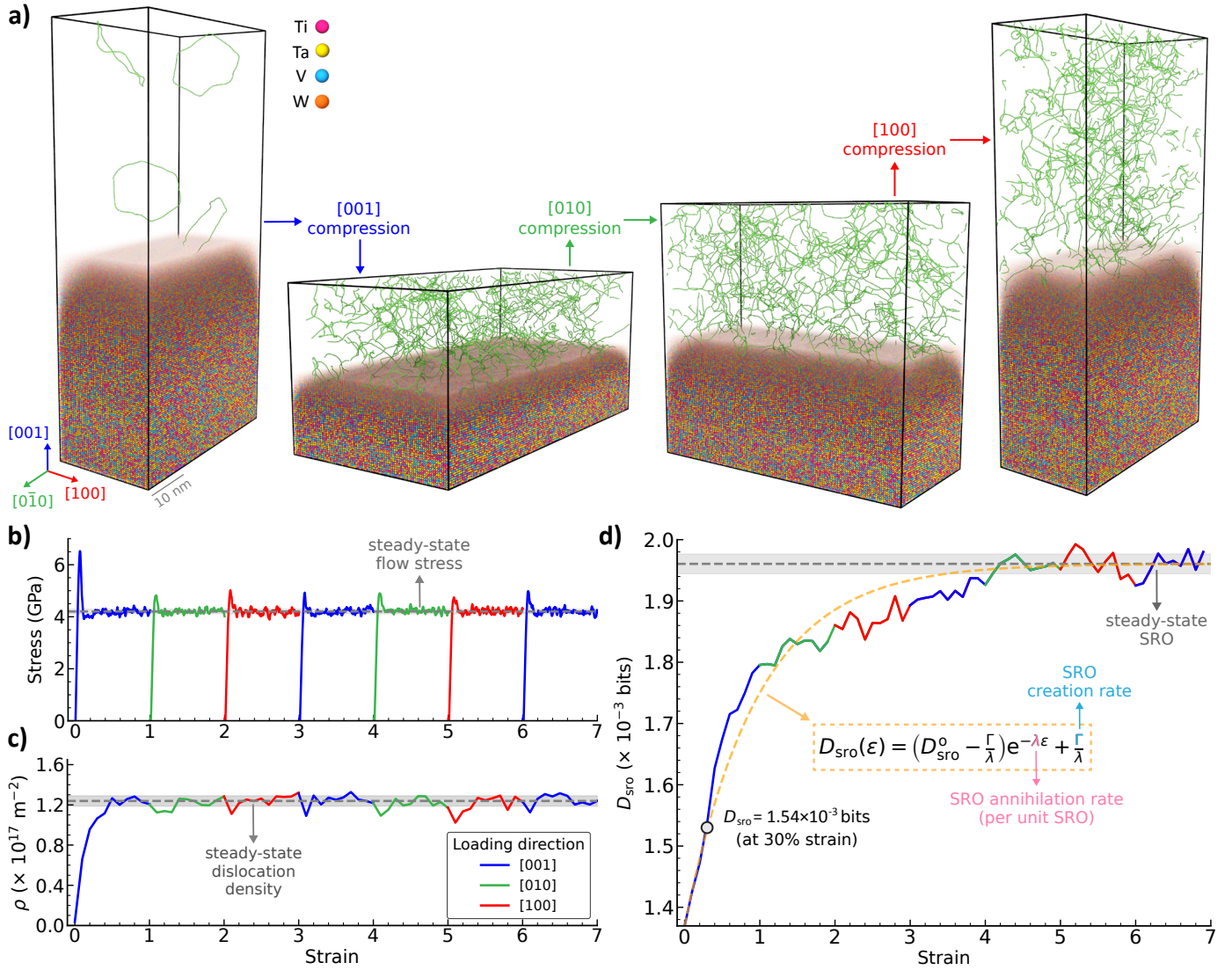


Figure 1: Thermomechanical processing of equiatomic TiTaVW alloy. **a)** Uniaxial compression of TiTaVW at 300 K under a constant strain rate of 10^9 s^{-1} . After each unit strain, the deformation axis is rotated to align with the direction of largest dimension. Dislocation networks are shown as green lines. **b)** Stress-strain curve shows the onset of steady-state flow stress. **c)** Dislocation density also reaches steady-state with continued deformation. **d)** Evolution of SRO (D_{sro}) with strain, eventually reaching a steady-state SRO (D_{sro}^{∞}). The dashed orange curve shows the fit to eq. 5, capturing the observed D_{sro} evolution.

mimics a “metal kneading” protocol⁵⁶. The crystal, initially shaped with a dimension ratio of 1:2:4, is compressed along its longest axis, and the process is repeated along the new longest dimension in each subsequent cycle, preserving nearly constant volume and minimizing artifacts due to periodic boundary conditions. The integration timestep of the simulations was set to 5 fs.

Dislocations in the systems were analyzed using the Dislocation Extraction Algorithm (DXA)⁵⁷. Prior to dislocation analysis, the atomic structures were denoised using a score-based denoising algorithm⁵⁸ for 8 steps. The cumulative edge-to-screw character ratio of dislocations in each simulation was quantified using the following expression:

$$R = \frac{\sum_i |\sin(\theta_i)| L_i}{\sum_i |\cos(\theta_i)| L_i}, \quad (1)$$

where θ_i is the angle between the line direction ℓ_i and the Burgers vector \mathbf{b}_i for dislocation segment i , and L_i is the length of that segment. In essence, R represents a length-weighted ratio of edge to screw character across all dislocation segments in the system.

All visualizations were performed using the Open Visualization Tool (OVITO)⁵⁹.

2.3. Annealing simulations

To compare the SRO states obtained from TMP simulations with those resulting from equilibrium processing pathways (i.e., annealing), we performed Monte Carlo simulations to thermally equilibrate chemical configurations of equiatomic TiTaVW over a wide temperature range. Simulations were conducted from 500 K to 10,000 K in 500 K increments. At each temperature, 65 independent simu-

lations were performed, each containing 4,394 atoms arranged in a cubic bcc cell of size $13a_o \times 13a_o \times 13a_o$ oriented along the [100], [010], and [001] directions, where a_o is the temperature-dependent lattice parameter. For temperatures above the melting point, a_o was determined by extrapolating its linear dependence on temperature. Periodic boundary conditions were applied in all directions.

Simulations were initialized with a random equiatomic distribution of atoms on the bcc lattice. Thermal equilibration was achieved through atom-swap attempts between atoms of different elements, with acceptance governed by the Metropolis criterion^{60,61} probability $\exp(-\Delta E/k_B T)$, where ΔE is the energy change associated with the swap, k_B is the Boltzmann constant, and T is the temperature. Each simulation was carried out for 360,000 steps (i.e., 80 swaps per atom), with the first 180,000 steps used for initial equilibration. Seven statistically uncorrelated configurations were sampled every 30,000 steps during the remaining 180,000 steps, yielding equilibrium SRO states analogous to those obtained from thermal annealing.

2.4. SRO quantification

To quantify chemical SRO in the states obtained from both TMP and annealing simulations, we employed the chemical motif framework introduced in refs. 14 and 15. In this approach, the local chemical environment of an atom was described by a motif \mathcal{M}_i , consisting of the atom and its first-nearest neighbors. We utilized the Euclidean graph neural network architecture⁶² from ref. 15 to identify all motifs \mathcal{M}_i in a system and compute their population density distributions $P(\mathcal{M}_i)$, hereafter denoted simply as P for brevity. The difference in SRO between two states, characterized by motif population density distributions P_1 and P_2 , was quantified using the Jensen-Shannon divergence:

$$D_{\text{JS}}(P_1 \parallel P_2) = \frac{1}{2}D_{\text{KL}}(P_1 \parallel M) + \frac{1}{2}D_{\text{KL}}(P_2 \parallel M), \quad (2)$$

where $M = \frac{1}{2}(P_1 + P_2)$ and D_{KL} denotes the Kullback-Leibler divergence⁶³. Larger values of $D_{\text{JS}}(P_1 \parallel P_2)$ indicate greater differences between P_1 and P_2 .

While eq. 2 can be used to compare two SRO states, it is often also desirable to quantify the absolute amount of SRO present in a single state. Here, this will be performed by measuring the divergence between the state of interest and a chemically random solid solution. For a state with motif population distribution P this is computed as

$$D_{\text{sro}} = D_{\text{JS}}(P \parallel P_{\text{rss}}), \quad (3)$$

where P_{rss} is the motif population density distribution of a chemically random solid solution. Larger values of D_{sro} indicate a greater absolute amount of SRO in the state defined by P .

For annealing simulations, P was evaluated using data from all seven snapshots across each of the 65 independent Monte Carlo runs described in section 2.3 (i.e., $7 \times 65 \times 4,394 = 1,999,270$ motifs per temperature). For TMP simulations, structures were first denoised using a

score-based denoising algorithm⁵⁸ for 8 steps. This was followed by identification of the crystal structure using the polyhedral template matching (PTM) algorithm with a root-mean-square deviation cutoff of 0.1. Only atoms identified as bcc were considered for constructing P . In both cases, P was generated by randomly sampling subsets of 1,900,000 motifs to ensure consistency across datasets.

To determine whether SRO states obtained from TMP are distinguishable from equilibrium configurations, we adopted the methodology developed in ref. 1. In this approach, the Jensen-Shannon divergence (eq. 2) between a nonequilibrium motif distribution P (obtained from TMP simulations) and all equilibrium distributions $P_{\text{eq}}(T)$ (obtained from annealing simulations) are computed. The minimum value among these, denoted D_{eff} , represents the distance of a nonequilibrium state from its closest equilibrium counterpart. States with D_{eff} that fall within their expected equilibrium baseline are classified as quasi-equilibrium states, whereas those that deviate are considered far-from-equilibrium states.

Additional quantification of SRO was obtained using the widely employed Warren-Cowley (WC) parameters⁶⁴, defined for each atomic pair AB as:

$$\alpha_{AB} = 1 - \frac{p(A|B)}{c_A}, \quad (4)$$

where $p(A|B)$ is the conditional probability of finding an A atom at a nearest-neighbor site of a B atom, and c_A is the average concentration of element A in the alloy.

3. Results

3.1. Thermomechanical processing-induced SRO

The stress-strain relationship for a representative processing condition ($T = 300$ K and $\dot{\epsilon} = 10^9$ s⁻¹) of the TiTaVW TMP simulations is shown in fig. 1b. The stress-strain curve begins with a clear elastic region, where stress increases linearly with strain up to the yield stress, at which point the four initially seeded dislocation loops begin to move, initiating plastic deformation. Soon after yielding, the system reaches a plateau in which the flow stress fluctuates around a steady mean (i.e., steady-state flow stress). Aside from brief transients caused by changes in the loading direction, the steady flow stress remains consistent throughout the seven deformation cycles. A similar trend is observed in the evolution of dislocation density (fig. 1c), where the steady-state dislocation density ρ^∞ is on the order of 10^{17} m⁻². This value is consistent with previous molecular dynamics simulation results^{55,56} and with theoretical estimates of the limiting dislocation density⁶⁵. The steady behavior in both flow stress and dislocation density is observed across all temperature and strain rate conditions considered in here, suggesting that it is a fundamental aspect of the alloy's thermomechanical response, when dislocations serve as the primary carriers of plasticity⁵⁶.

To examine how the SRO of the material evolves under such deformation, we monitored D_{sro} (eq. 3) as a function of strain, as illustrated in fig. 1d. With plastic deforma-

tion, the initially chemically random system forms SRO, evidenced by a rapid increase in D_{sro} with strain. Remarkably, even at a strain of 0.3, substantial SRO has already formed, indicating that modest levels of plastic strain — typical in many materials processing conditions — are sufficient to induce SRO in random solid solutions. This has important implications for interpreting the role of SRO on mechanical response during experiments: since SRO begins to evolve from the very onset of plastic deformation, even modest plastic strain can significantly alter the local chemical environment in the alloy⁶⁶. As a result, any subsequent mechanical testing will reflect a modified SRO state, complicating efforts to isolate direct influence of SRO on mechanical properties.

With continued deformation, the system eventually reaches a steady value of D_{sro} , denoted D_{sro}^∞ , that is independent of the initial SRO state before deformation, as demonstrated in ref. 1. This implies that even if we were to initialize the simulation with a more ordered configuration, such as a state annealed at moderate temperatures, the system would still evolve toward the same D_{sro}^∞ shown in fig. 1d. The evolution of D_{sro} with strain during TMP, across all processing conditions considered here, is well described by the following equation:

$$D_{\text{sro}}(\epsilon) = \left(D_{\text{sro}}^o - \frac{\Gamma}{\lambda} \right) e^{-\lambda\epsilon} + \frac{\Gamma}{\lambda}, \quad (5)$$

where D_{sro}^o is the initial amount of SRO, and Γ and λ are rate parameters governing the SRO evolution kinetics. Note that $D_{\text{sro}}^\infty = D_{\text{sro}}(\epsilon \rightarrow \infty) = \Gamma/\lambda$, from to eq. 5. For the specific case shown in fig. 1d ($T = 300\text{ K}$ and $\dot{\epsilon} = 10^9\text{ s}^{-1}$), the values of Γ and λ are 2.02×10^{-3} bits per unit strain and 1.03 per unit strain, respectively.

Taking the derivative of eq. 5 with respect to strain yields the following SRO evolution equation:

$$\frac{d}{d\epsilon}(D_{\text{sro}}) = \Gamma - \lambda D_{\text{sro}}. \quad (6)$$

The two terms on the right-hand side of eq. 6 reveal the existence of two competing processes governing the SRO evolution¹. The first term (Γ) is positive and represents the rate of SRO creation, arising from the inherent chemical bias associated with dislocation motion. Driven by applied mechanical forces, dislocations preferentially traverse through low-energy pathways. The energetics of these pathways are dictated by the local chemical motifs near the dislocation core^{1,30}. As a result, dislocation motion in metallic alloys is chemically selective and promotes the formation of SRO by favoring certain motifs over others. The second term ($-\lambda D_{\text{sro}}$) is negative and proportional to the amount of SRO present in the system; it accounts for the destruction of SRO due to the randomizing effects of the mechanically-biased component of dislocation motion. Together, the SRO creation rate Γ and annihilation rate λ govern the overall evolution of SRO during TMP.

3.2. Effects of processing conditions on steady-state SRO

We now turn our attention to the steady-states of SRO induced by TMP. Figure 2a shows the steady-state SRO (D_{sro}^∞) under a wide range of processing conditions. It is evident that both temperature and strain rate have systematic effects on D_{sro}^∞ . At low temperatures (300 K–1,100 K), D_{sro}^∞ remains small, with only a weak positive correlation with temperature. Extrapolating this observation (sec. 3.5) to even lower temperatures approaching 0 K shows that a finite degree of SRO persists, even in the absence of any thermal activation, due to chemical biases in the athermal and deformation-driven chemical mixing. Within this low-temperature regime, reducing the strain rate by an order of magnitude has little effect on D_{sro}^∞ . A stronger positive correlation between D_{sro}^∞ and temperature emerges in the moderate temperature range (1,300–1,500 K), where thermally activated dislocation mechanisms start to dominate. Beyond this regime, D_{sro}^∞ increases rapidly with temperature. In this high-temperature regime, a pronounced strain rate dependence also emerges: slower deformation rates lead to larger D_{sro}^∞ . This trend indicates that chemical mixing driven by thermally-activated dislocation motion, when combined with slower mechanical driving (which allows more time for atomic rearrangement), promotes the formation of SRO.

Since TMP is a nonequilibrium process, the resulting SRO states are likewise nonequilibrium in nature. We quantify their deviation from equilibrium configurations using D_{eff} (sec. 2.4), a metric that measures the statistical distance between a steady-state SRO configuration and its corresponding equilibrium counterpart using eq. 2. Larger D_{eff} values indicate greater deviations from equilibrium. As shown in fig. 2b, D_{eff} increases monotonically with temperature, implying that thermal activation of dislocation motion drives the system progressively further from equilibrium SRO. In equilibrium states, D_{eff} values are expected to remain below 1.52×10^{-3} bits. However, as indicated in fig. 2b, the steady-states of SRO obtained through TMP consistently exceed this threshold, confirming their far-from-equilibrium character. These far-from-equilibrium SRO states, observed during TMP, cannot be accessed via equilibrium pathways such as thermal annealing. As a result, TMP opens a new regime of SRO states beyond the traditional equilibrium space.

Finally, the modulation of steady-state SRO by TMP parameters is also reflected in their pairwise chemical preferences. Figure 2c shows the WC parameters (eq. 4) for all atomic pairs as functions of temperature and strain rate. The overall trend parallels that of fig. 2a: increasing the temperature increases the degree of SRO. However, a particularly intriguing feature is observed — namely, shifts in chemical pair preferences around 1,300 K–1,500 K. Specifically, Ti–Ti, Ta–V, and V–V exhibit distinct transitions across this temperature range, shifting from pair repulsion (positive WC parameters) to pair attraction (negative WC parameters). The temperature range over which this transition occurs aligns with the sharp rise in D_{sro}^∞ with

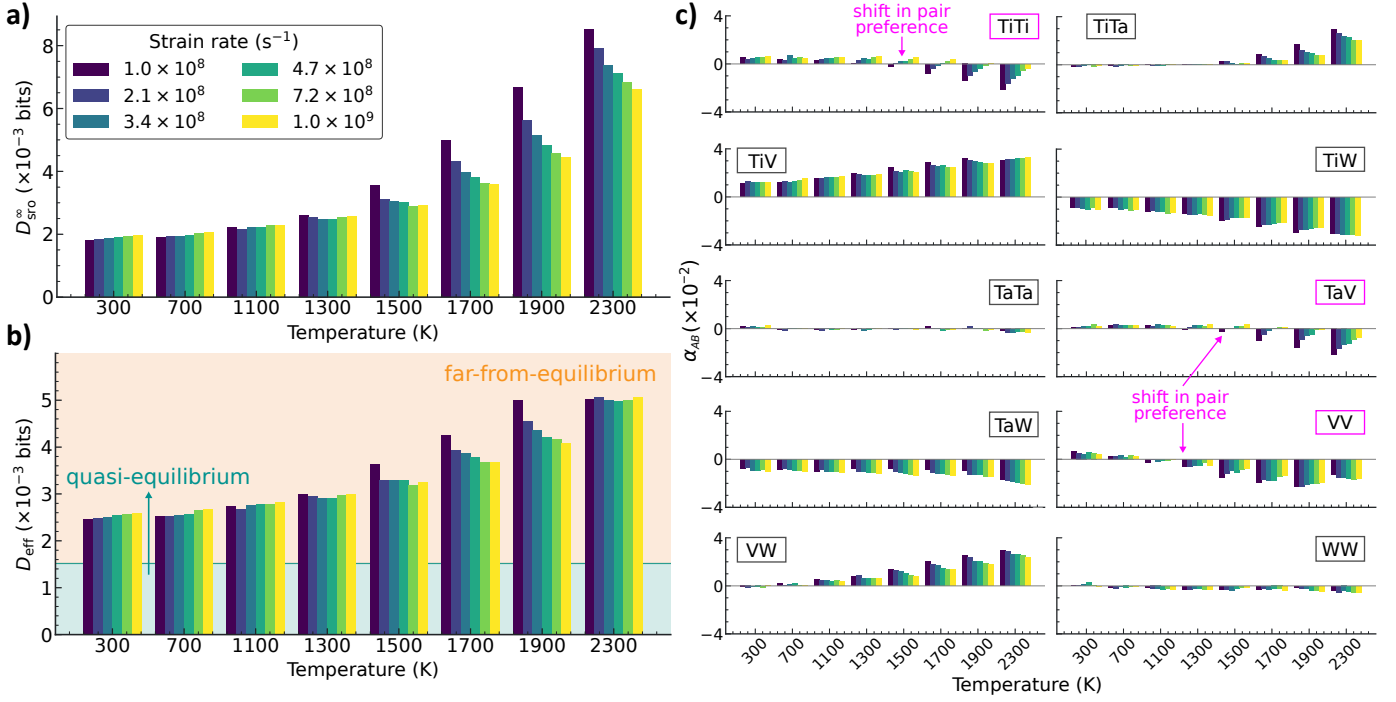


Figure 2: Effect of temperature and strain rate on steady-state SRO. a) Steady-state SRO (D_{sro}^{∞}) as a function of temperature and strain rate. b) The steady-state SRO states are of far-from-equilibrium kind¹ and they move further from equilibrium as temperature increases, indicated by increasing D_{eff} (sec. 2.4) c) Warren-Cowley parameters for different pairs indicate that there is a change in pair preference at moderate temperatures for certain elemental pairs (indicated by the purple box), marking a change in the chemical motifs forming the SRO.

temperature seen in fig. 2a, indicating that the activation of thermal processes not only amplifies the amount of SRO but also alters its underlying chemical nature.

3.3. Effects of processing conditions on SRO evolution rate

To investigate the effect of processing parameters on the evolution of SRO, we begin by examining how they influence the SRO creation (Γ) and annihilation (λ) rates introduced in section 3.1, which together govern SRO evolution rate with strain (eq. 6). The SRO creation rate Γ as a function of strain rate and temperature is shown in fig. 3a. At the low-temperature regime, the effect of temperature and strain rate on Γ is negligible. However, in the range of 1,100 K–1,500 K, we observe that Γ increases rapidly with temperature. A strain rate dependence also emerges in this regime, with lower strain rates resulting in higher values of Γ . Notably, the temperature at which this transition — from processing condition-insensitive to processing condition-sensitive behavior — occurs appears to be itself strain-rate dependent, gradually shifting to lower temperatures as the strain rate decreases. The SRO annihilation rate (λ) exhibits a qualitatively similar trend, as shown in fig. 3b. However, the transition in λ occurs at slightly higher temperatures, approximately in the range of 1,500 K–1,700 K.

While both Γ and λ increase with temperature beyond their respective transition points, their functional forms differ markedly. Γ grows exponentially with tempera-

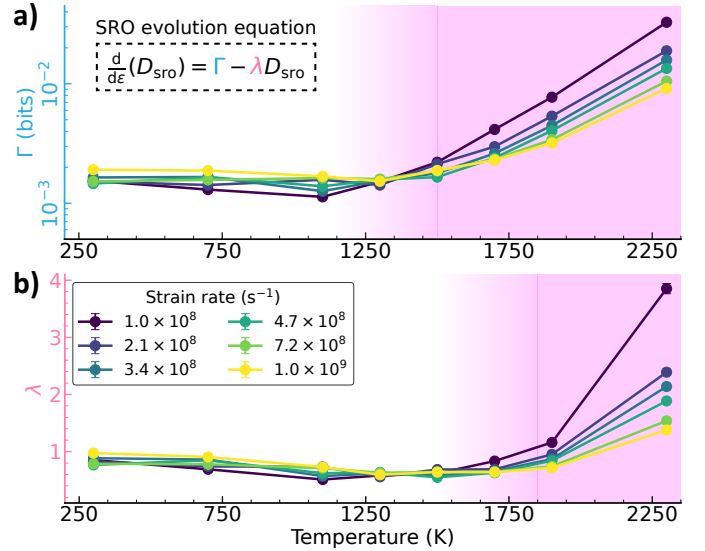


Figure 3: Effect of temperature and strain rate on SRO evolution rate. Temperature and strain rate dependence of a) SRO creation rate Γ , and b) SRO annihilation rate λ . The shaded purple region highlights the temperature range where both Γ and λ become sensitive to changes in temperature and strain rate. Error bars (one standard deviation) are smaller than the marker size and therefore not visible.

ture, increasing by one order of magnitude. In contrast, λ increases approximately in a linear fashion, remaining within the same order of magnitude across the tempera-

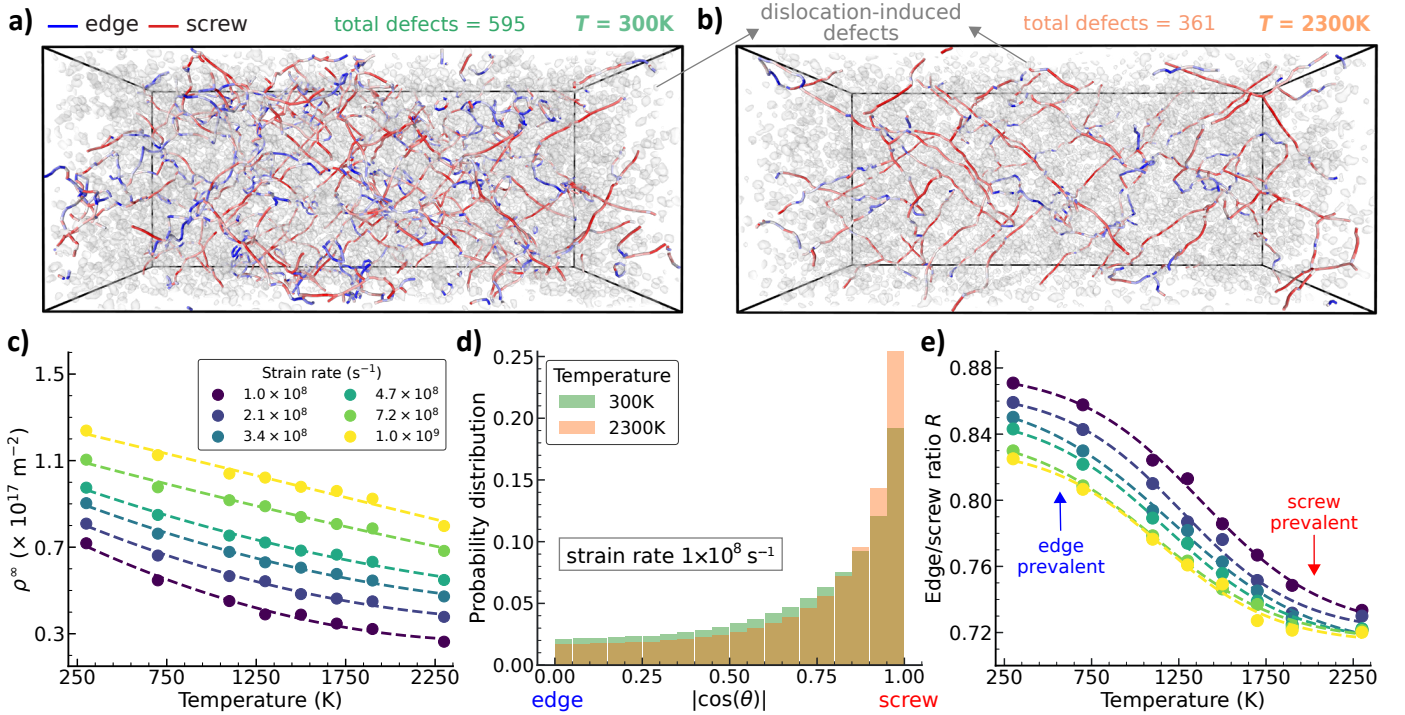


Figure 4: Dislocation-mediated mechanisms of SRO evolution. a) Dislocation configuration at 300 K and b) 2300 K after reaching steady state during thermomechanical processing at a strain rate of 10^8 s^{-1} . Grey features indicate dislocation-induced defects originating from cross-kinks (approximately 595 at 300 K and 361 at 2,300 K.) c) Steady-state dislocation density ρ^∞ decreases with temperature and strain rate. d) Probability distribution of dislocation character at $\dot{\epsilon} = 10^8 \text{ s}^{-1}$, where θ is the angle between the Burgers vector and line direction θ . e) Ratio of edge-to-screw character R (eq. 1) as a function of temperature and strain rate.

ture range studied. This difference between Γ and λ quantitatively explains the rapid increase in steady-state SRO ($D_{\text{SRO}}^\infty = \Gamma/\lambda$), observed at high temperatures (fig. 2a). Moreover, because λ also appears in the exponential term of eq. 5, its increase with temperature shortens the characteristic strain scale for SRO evolution, allowing the system to reach steady-state SRO more rapidly (i.e., over a smaller strain interval).

The dependence of the transition temperature of both Γ and λ on strain rate, observed in fig. 3, has important implications. Since control of SRO evolution via temperature becomes feasible only beyond the transition temperature, the ability to tune the transition temperature through strain rate provides a valuable degree of process control. Specifically, by sufficiently reducing the strain rate, the transition can be shifted to lower temperatures, thereby enabling SRO control under more accessible and experimentally achievable TMP conditions.

3.4. Effects of processing conditions on SRO evolution mechanism

Having established that processing parameters can modulate the SRO creation and annihilation rates — and consequently, SRO evolution — we now turn to the underlying mechanisms responsible for this control. As explained in section 3.1, SRO formation during TMP occurs due to the chemical bias associated with dislocation motion¹. Any

phenomenon during deformation that enhances this chemical bias promotes SRO creation, while phenomena that counteract it contribute to SRO annihilation.

We first examine the role of steady-state dislocation density ρ^∞ in modulating the chemical bias. A dense dislocation network restricts dislocation mobility through elastic interactions, geometrical constraints, and dislocation junctions. These constraints are evident in the dislocation configuration shown in fig. 4a, which corresponds to the processing condition of $T = 300 \text{ K}$ and $\dot{\epsilon} = 10^8 \text{ s}^{-1}$. The dislocations appear highly entangled, forming dense forests that inhibit their motion. In contrast, the dislocation configuration in fig. 4b, corresponding to $T = 2300 \text{ K}$ at the same strain rate, contains fewer dislocations, allowing for the formation of longer, more mobile dislocation lines. The grey features visible in both systems represent dislocation-induced defects such as vacancies, interstitials, and defect clusters. These defects originate primarily from the self-pinning of screw dislocations, a consequence of kink-pair nucleation on intersecting glide planes^{11,67}. Such defects are notably more prevalent in the system shown in fig. 4a than in fig. 4b (i.e., 64% more defects at 300 K than 2,300 K), further impeding dislocation motion, especially of screw types. Together, these constraints limit the number of energetically distinct pathways accessible to dislocations, thereby suppressing the manifestation of chemical bias in their motion. As a result, *elevated dislocation den-*

sities and defect concentrations reduce the extent of SRO formation.

Figure 4c shows the variation of ρ^∞ with strain rate and temperature. At low temperatures, ρ^∞ is high, and, for a given temperature, higher strain rates result in higher ρ^∞ . Low temperatures also result in a larger number of dislocation-induced defects, as there is not enough thermal energy to overcome the cross-kinks. This explains the trends observed in fig. 3a, where the SRO creation rate Γ increases with temperature. The origin of this increase lies, in part, in the reduction of ρ^∞ (and associated defects) at elevated temperatures. Similarly, the enhancement of SRO formation at lower strain rates can be attributed to the corresponding decrease in ρ^∞ . Lower strain rates also provide more time for dislocations to sample available paths and preferentially select energetically favorable ones, further promoting chemically biased dislocation motion. The increased dislocation mobility at higher temperatures also contributes to the rise in the SRO annihilation rate λ (fig.3b) by enabling more frequent interactions between dislocations and chemical motifs. However, this increase is considerably less pronounced than the corresponding rise in Γ (fig.3a).

While the restrictive influence of dislocation forests and dislocation-induced defects accounts for much of the observed temperature and strain rate dependence, it does not fully explain the discernible transition in SRO evolution behavior at moderate temperatures (fig. 3) or the weak strain rate sensitivity observed at low temperatures. To resolve this, we examine the character of the dislocations present in the system and its temperature dependence. It is well established that at low temperatures, screw dislocations are considerably less mobile than their edge counterparts²⁹ — a difference that diminishes as temperature increases. The higher concentration of self-pinning features at lower temperatures (fig. 4a) is itself a manifestation of this behavior. In addition, fig. 4d shows that increasing temperature leads to a significant shift in the overall dislocation character toward screw. This phenomenon can be directly visualized in figs. 4a and 4b, where it is clear that the system deformed at 300 K possesses a larger fraction of edge dislocations compared to 2300 K. This overall shift toward a screw-dominated dislocation population at elevated temperatures, combined with their increased mobility, is mechanistically significant.

Among dislocation types, screw dislocations are more chemically biased in their motion. This is due to their ability to move via kink-pair formation and cross-slip. These mechanisms allow screw dislocations to sample numerous transition pathways, *making their mobility more sensitive to the local chemical environment*. In contrast, edge dislocations are confined mostly to fixed glide planes, rendering their motion less dependent on chemistry (i.e., more mechanically driven). This distinction has been observed in ref. 29, where screw dislocation mobility was shown to depend sensitively on the local chemical ordering, whereas edge dislocation mobility remained largely unaffected.

Figure 4e shows a transition toward reduced ratio of

edge-to-screw character R (eq. 1) at moderate temperatures. As R decreases, the overall chemical bias of dislocation motion is amplified (due to decreased edge character), leading to enhanced SRO formation. This trend (along with the decrease in ρ^∞) accounts for the observed increase in the SRO creation rate Γ (fig. 3a) in this regime, causing it to outpace the annihilation rate λ increase (fig. 3b). A particularly revealing aspect of the effect of dislocation character emerges when examining low-temperature conditions. Here, high strain rates produce two competing effects: they increase ρ^∞ and associated defects (suppressing SRO creation), while simultaneously decreasing R (promoting SRO creation). The net result of these opposing influences — enhanced chemical bias from reduced edge character versus restricted motion from higher ρ^∞ — explains the weak strain rate dependence of SRO evolution at low temperatures seen in fig. 3. The high-temperature regime presents a different dynamic. As fig. 4e demonstrates, variations in strain rate have progressively less effect on R at elevated temperatures. In this regime, ρ^∞ remains the dominant factor: lower strain rates lead to reduced densities and, consequently, enhanced SRO formation.

3.5. Process-space extrapolation of steady-state SRO

The processing conditions investigated here correspond to high strain-rate deformation, characteristic of processes such as laser-induced shock or ablation^{68,69}. Nevertheless, our results can be extrapolated to predict steady-state SRO (D_{sro}^∞) in lower strain-rate regimes more relevant to conventional materials processing. To enable such extrapolation we introduce the following empirical model:

$$D_{\text{sro}}^\infty(T, \dot{\epsilon}) = D_{\text{sro}}^{\text{ath}}(\dot{\epsilon}) + \frac{D_{\text{sro}}^{\text{sat}}(\dot{\epsilon}) - D_{\text{sro}}^{\text{ath}}(\dot{\epsilon})}{1 + e^{-w[T - T_o(\dot{\epsilon})]}}. \quad (7)$$

Each parameter in this model has a well-defined physical interpretation that will be discussed next. As shown in fig. 5a, at the low-temperature limit, D_{sro}^∞ reaches a finite minimum, indicating the persistence of steady-state SRO even in the absence of any thermal activation. We refer to this residual SRO as athermal SRO $D_{\text{sro}}^{\text{ath}}$. At the high-temperature end of fig. 5a, D_{sro}^∞ approaches a saturation value that we call saturation SRO $D_{\text{sro}}^{\text{sat}}$. The transition temperature marking the onset of rapid SRO increase with temperature is denoted as T_o , while the parameter w governs the sharpness of this transition. All model parameters, except for w , exhibit a linear dependence on the logarithm of strain rate. Despite its simplicity, this empirical model provides an excellent fit to the simulation data (fig. 5a), enabling valid extrapolation to a broader range of processing conditions.

To place the steady-state SRO obtained from TMP in an equilibrium thermodynamic context, we map each state to its equilibrium counterpart based on SRO magnitude. This requires first understanding how the equilibrium SRO varies with temperature. As shown in fig. 5b, the equilibrium SRO exhibits a transition from long-range to short-

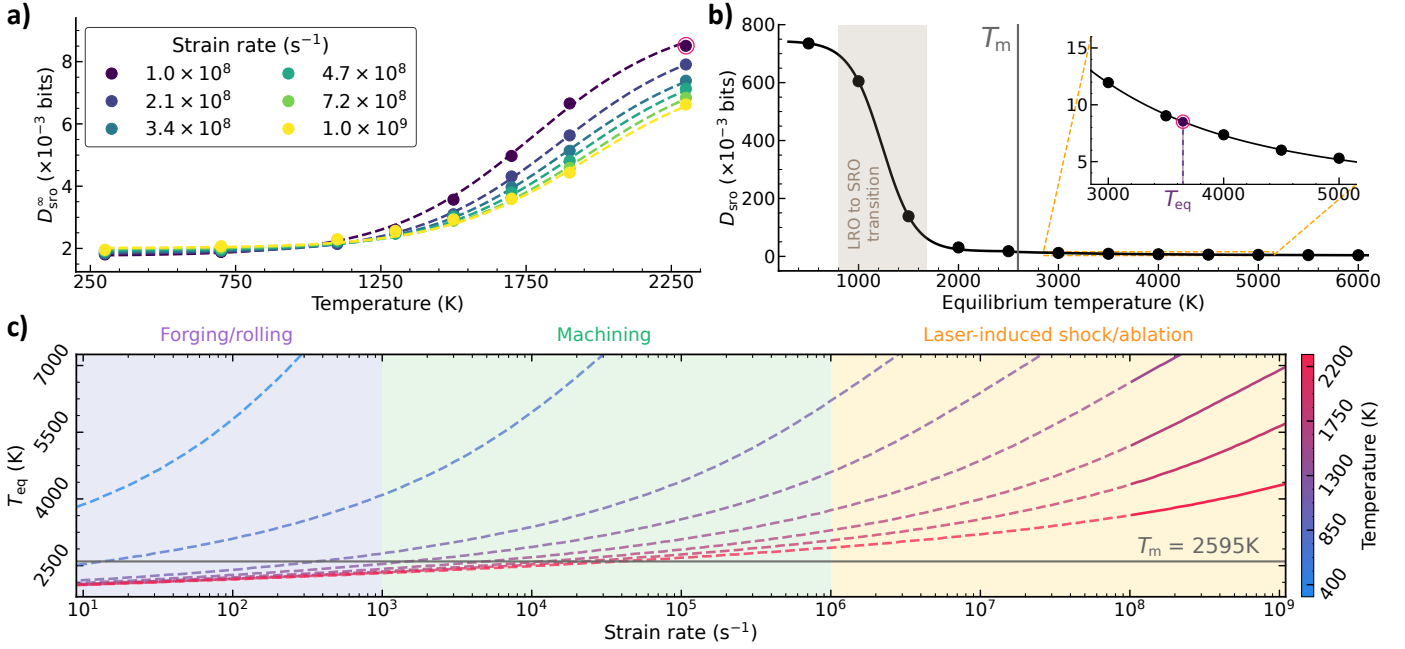


Figure 5: Steady-state SRO during manufacturing processes. **a)** The variation of steady-state SRO D_{sro}^{∞} induced by thermomechanical processing as a function of temperature and strain rate. The dashed lines show the empirical model (eq. 7) fit to the data. **b)** Equilibrium SRO states obtained from annealing at different temperatures. The equivalent temperature, T_{eq} , is determined by matching D_{sro}^{∞} obtained from thermomechanical processing with its corresponding equilibrium SRO value. An example match is highlighted by the magenta circled markers; the corresponding T_{eq} is indicated by the vertical dashed line in the inset. **c)** Map of T_{eq} across a wide range of temperatures and strain rates, spanning three relevant manufacturing process categories. The dashed line segments indicate extrapolated values obtained from the empirical model.

range order between 1,000 K-1,500 K, followed by a gradual decrease with temperature (fig. 5b inset). Notably, the SRO never vanishes, even beyond the melting point ($T_m = 2595$ K). For each thermomechanical condition, we define an equivalent temperature, T_{eq} , as the equilibrium temperature at which the equilibrium SRO most closely matches D_{sro}^{∞} . This mapping, illustrated in fig. 5b inset, provides a thermodynamically meaningful framework for interpreting processing-mediated SRO.

Using the empirical model (eq. 7), we extrapolate D_{sro}^{∞} to slower strain rates and construct a corresponding map of T_{eq} across a wide range of processing conditions in fig. 5c. The extrapolated strain-rate regimes are illustrated by three representative manufacturing process categories: forging/rolling^{70,71}, machining^{72,73}, and laser-induced shock/ablation^{68,69}. Figure 5c demonstrates that each of these categories can access a broad spectrum of SRO states, including states with T_{eq} well below the melting point. For example, under a strain rate typical of forging/rolling (20 s^{-1}) at a deformation temperature of 1100 K, the TiTaVW alloy can reach a steady-state SRO comparable in magnitude to the SRO state obtained by annealing at 2,200 K. However, as discussed in section 3.2, the chemical nature of these two SRO states would be fundamentally different.

It is important to note that our simulations were conducted at high strain rates, where diffusion-based mechanisms such as dislocation climb and point-defect migration are largely suppressed. Among these, vacancy mi-

gration is known to be responsible for SRO formation during equilibrium processes. As a result, the empirical model in eq. 7 will not capture the full contribution such diffusion-mediated mechanisms. At lower strain rates, longer timescales will allow these mechanisms to become active⁷⁴, potentially enhancing SRO further and consequently lowering T_{eq} beyond the predictions of our model. Thus, the T_{eq} values shown in fig. 5c, particularly at low strain rates, should be interpreted as conservative upper bounds estimates. In practice, even higher degrees of SRO may be attainable through TMP. This underscores the potential of TMP as a practical route for achieving targeted SRO states.

4. Conclusion

Building on our previous finding that dislocation motion both creates and destroys SRO, driving alloys into far-from-equilibrium states¹, we demonstrate here that during TMP the evolution of SRO follows a quantitative balance between creation and annihilation rates, Γ and λ , and we quantify how this balance varies with temperature and strain rate. We further explain this dependence through physical features of the dislocation network — dislocation density, edge-to-screw ratio, and the population/annealing of cross-kink-induced defects — which together govern the degree of chemically biased versus mechanically biased dislocation motion.

By systematically varying the processing conditions

(temperature and strain rate), we identified two distinct regimes of SRO evolution. At low temperatures, high dislocation density and abundant dislocation-induced defects limit mobility and suppress SRO creation, yet the strain-rate dependence remains weak due to compensating changes in dislocation character. At moderate to high temperatures, thermally activated mechanisms reduce dislocation density and shift the dislocation population toward screw character, amplifying chemical bias and sharply increasing Γ relative to λ . This mechanistic transition explains the strong temperature and strain rate sensitivity of steady-state SRO observed in this regime.

The steady-state SRO states reached under TMP are far-from-equilibrium¹, lying outside the range accessible by thermal annealing and thus expanding the accessible SRO landscape. The framework established here — linking processing parameters to Γ and λ through measurable dislocation properties — provides a physically grounded, transferable basis for understanding and predicting SRO evolution in chemically complex alloys. While the present results are derived from high-strain-rate atomistic simulations of a refractory high-entropy alloy, the mechanistic connections identified between dislocation density, character, and chemical bias are general, offering a route to integrate SRO evolution into broader models of microstructural development under TMP. Perhaps more importantly, the mechanistic basis for SRO evolution derived here is testable with diffraction, dislocation analysis, and chemical-correlation measurements during controlled TMP.

Data and code availability

The software for SRO quantification can be found in our `ChemicalMotifIdentifier` Python package⁷⁵. The machine learning potential can be found in our `Machine-learning-potentials-for-modeling-alloys-across-compositions` GitHub repository⁷⁶. Our figure style is implemented in `LovelyPlots`⁷⁷ under the `paper` style. Any custom code or data that is not currently available in these repositories can be subsequently added upon reasonable request to the corresponding author.

CRediT author statement

Mahmudul Islam: Conceptualization, Methodology, Data Curation, Formal Analysis, Investigation, Software, Visualization, Writing – Original Draft. **Killian Sheriff:** Conceptualization, Methodology, Software, Formal Analysis, Investigation, Writing – Review & Editing. **Rodrigo Freitas:** Conceptualization, Supervision, Project Administration, Funding Acquisition, Resources, Writing – Review & Editing.

Acknowledgments

This material is based upon work supported by the Air Force Office of Scientific Research (AFOSR) under award number FA9550-25-1-0199, through the Young Investigator Program. This work was also supported by the MathWorks Ignition Fund and MathWorks Engineering Fellowship Fund and the Exponent Fellowship. This research

used resources of the Oak Ridge Leadership Computing Facility’s Frontier supercomputer at Oak Ridge National Laboratory, supported by the Office of Science of the U.S. Department of Energy under Contract No. DE-AC05-00OR22725, through an award from the INCITE program. Allocation of compute time was provided by the DOE Innovative and Novel Computational Impact on Theory and Experiment (INCITE) Program. The authors thank Vasily Bulatov and Nicolas Bertin of Lawrence Livermore National Laboratory for their valuable discussions.

Competing interests

The authors declare no competing interests.

5. References

- [1] Mahmudul Islam, Killian Sheriff, Yifan Cao, and Rodrigo Freitas, *Nonequilibrium chemical short-range order in metallic alloys*, 3, 2025, DOI: [10.48550/arXiv.2409.15474](https://doi.org/10.48550/arXiv.2409.15474), arXiv: [2409.15474](https://arxiv.org/abs/2409.15474)[cond-mat].
- [2] J. Rackwitz, G. B. Olson, and C. C. Tasan, “Understanding thermo-mechanical processing pathways to simultaneously increase strength and damping in steels”, *Acta Materialia* (1, 2025), DOI: [10.1016/j.actamat.2025.120864](https://doi.org/10.1016/j.actamat.2025.120864).
- [3] Bernhard Trink, Irmgard Weissensteiner, Peter J. Uggowitzer, Katharina Strobel, Anna Hofer-Roblyek, and Stefan Pogatscher, “Processing and microstructure–property relations of Al–Mg–Si–Fe crossover alloys”, *Acta Materialia* (15, 2023), DOI: [10.1016/j.actamat.2023.119160](https://doi.org/10.1016/j.actamat.2023.119160).
- [4] Kenta Yamanaka, Manami Mori, Shigeo Sato, and Akihiko Chiba, “Stacking-fault strengthening of biomedical Co–Cr–Mo alloy via multipass thermomechanical processing”, *Scientific Reports* (7, 2017), DOI: [10.1038/s41598-017-10305-1](https://doi.org/10.1038/s41598-017-10305-1).
- [5] Yonghao Sun, Amadeu Concustell, and A. Lindsay Greer, “Thermomechanical processing of metallic glasses: extending the range of the glassy state”, *Nature Reviews Materials* (7, 2016), DOI: [10.1038/natrevmats.2016.39](https://doi.org/10.1038/natrevmats.2016.39).
- [6] B. Schuh, F. Mendez-Martin, B. Völker, E. P. George, H. Clemens, R. Pippan, and A. Hohenwarter, “Mechanical properties, microstructure and thermal stability of a nanocrystalline CoCrFeMnNi high-entropy alloy after severe plastic deformation”, *Acta Materialia* (1, 2015), DOI: [10.1016/j.actamat.2015.06.025](https://doi.org/10.1016/j.actamat.2015.06.025).
- [7] Hamed Shahmir, Junyang He, Zhaoping Lu, Megumi Kawasaki, and Terence G. Langdon, “Effect of annealing on mechanical properties of a nanocrystalline CoCrFeNiMn high-entropy alloy processed by high-pressure torsion”, *Materials Science and Engineering: A* (31, 2016), DOI: [10.1016/j.msea.2016.08.118](https://doi.org/10.1016/j.msea.2016.08.118).
- [8] Q. Rizzardi, C. McElfresh, G. Sparks, D. D. Stauffer, J. Marian, and R. Maaß, “Mild-to-wild plastic transition is governed by athermal screw dislocation slip in bcc Nb”, *Nature Communications* (23, 2022), DOI: [10.1038/s41467-022-28477-4](https://doi.org/10.1038/s41467-022-28477-4).
- [9] R. E. Kubilay, A. Ghafarollahi, F. Maresca, and W. A. Curtin, “High energy barriers for edge dislocation motion in body-centered cubic high entropy alloys”, *npj Computational Materials* (19, 2021), DOI: [10.1038/s41524-021-00577-7](https://doi.org/10.1038/s41524-021-00577-7).
- [10] Yan Lu, Yu-Heng Zhang, En Ma, and Wei-Zhong Han, “Relative mobility of screw versus edge dislocations controls the ductile-to-brittle transition in metals”, *Proceedings of the National Academy of Sciences* (14, 2021), DOI: [10.1073/pnas.2110596118](https://doi.org/10.1073/pnas.2110596118).
- [11] Jaime Marian, Wei Cai, and Vasily V. Bulatov, “Dynamic transitions from smooth to rough to twinning in dislocation motion”, *Nature Materials* (2004), DOI: [10.1038/nmat1072](https://doi.org/10.1038/nmat1072).
- [12] Vasily Bulatov and Wei Cai, *Computer Simulations of Dislocations*, OUP Oxford, 2, 2006, ISBN: 978-0-19-852614-8.
- [13] Haidong Fan, Qingyuan Wang, Jaafar A. El-Awady, Dierk Raabe, and Michael Zaiser, “Strain rate dependency of dislocation plasticity”, *Nature Communications* (23, 2021), DOI: [10.1038/s41467-021-21939-1](https://doi.org/10.1038/s41467-021-21939-1).
- [14] Killian Sheriff, Yifan Cao, Tess Smidt, and Rodrigo Freitas, “Quantifying chemical short-range order in metallic alloys”, *Proceedings of the National Academy of Sciences* (18, 2024), DOI: [10.1073/pnas.2322962121](https://doi.org/10.1073/pnas.2322962121).
- [15] Killian Sheriff, Yifan Cao, and Rodrigo Freitas, “Chemical-motif characterization of short-range order with E(3)-equivariant graph neural networks”, *npj Computational Materials* (2024), DOI: [10.1038/s41524-024-01393-5](https://doi.org/10.1038/s41524-024-01393-5).
- [16] Lingling Zhou, Qi Wang, Jing Wang, Xuefei Chen, Ping Jiang, Hao Zhou, Fuping Yuan, Xiaolei Wu, Zhiying Cheng, and En Ma, “Atomic-scale evidence of chemical short-range order in CrCoNi medium-entropy alloy”, *Acta Materialia* (1, 2022), DOI: [10.1016/j.actamat.2021.117490](https://doi.org/10.1016/j.actamat.2021.117490).
- [17] E. Antillon, C. Woodward, S. I. Rao, and B. Akdim, “Chemical short range order strengthening in BCC complex concentrated alloys”, *Acta Materialia* (15, 2021), DOI: [10.1016/j.actamat.2021.117012](https://doi.org/10.1016/j.actamat.2021.117012).
- [18] E. Antillon, C. Woodward, S. I. Rao, B. Akdim, and T. A. Parthasarathy, “Chemical short range order strengthening in a model FCC high entropy alloy”, *Acta Materialia* (15, 2020), DOI: [10.1016/j.actamat.2020.02.041](https://doi.org/10.1016/j.actamat.2020.02.041).
- [19] Sriswaroop Dasari, Abhishek Sharma, Chao Jiang, Bharat Gwalani, Wei-Chih Lin, Kai-Chi Lo, Stéphane Gorsse, An-Chou Yeh, Srivilliputhur G. Srinivasan, and Rajarshi Banerjee, “Exceptional enhancement of mechanical properties in high-entropy alloys via thermodynamically guided local chemical ordering”, *Proceedings of the National Academy of Sciences* (6, 2023), DOI: [10.1073/pnas.2211787120](https://doi.org/10.1073/pnas.2211787120).
- [20] Shuai Chen, Zachary H. Aitken, Subrahmanyam Pattamatta, Zhaoxuan Wu, Zhi Gen Yu, David J. Srolovitz, Peter K. Liaw, and Yong-Wei Zhang, “Simultaneously enhancing the ultimate strength and ductility of high-entropy alloys via short-range ordering”, *Nature Communications* (16, 2021), DOI: [10.1038/s41467-021-25264-5](https://doi.org/10.1038/s41467-021-25264-5).
- [21] Hui Zheng, Lauren T. W. Fey, Xiang-Guo Li, Yong-Jie Hu, Liang Qi, Chi Chen, Shuozhi Xu, Irene J. Beyerlein, and Shyue Ping Ong, “Multi-scale investigation of short-range order and dislocation glide in MoNbTi and TaNbTi multi-principal element alloys”, *npj Computational Materials* (30, 2023), DOI: [10.1038/s41524-023-01046-z](https://doi.org/10.1038/s41524-023-01046-z).
- [22] Zhengxiong Su, Jun Ding, Miao Song, Li Jiang, Tan Shi, Zhiming Li, Sheng Wang, Fei Gao, Di Yun, En Ma, and Chenyang Lu, “Enhancing the radiation tolerance of high-entropy alloys via solute-promoted chemical heterogeneities”, *Acta Materialia* (15, 2023), DOI: [10.1016/j.actamat.2022.118662](https://doi.org/10.1016/j.actamat.2022.118662).
- [23] O. El Atwani, H. T. Vo, M. A. Tunes, C. Lee, A. Alvarado, N. Krienke, J. D. Poplawsky, A. A. Kohnert, J. Gigax, W.-Y. Chen, M. Li, Y. Q. Wang, J. S. Wróbel, D. Nguyen-Manh, J. K. S. Baldwin, O. U. Tukac, E. Aydoğan, S. Fensin, and E. Martinez, “A quinary WTaCrVHf nanocrystalline refractory high-entropy alloy withholding

- extreme irradiation environments”, *Nature Communications* (2, 2023), DOI: [10.1038/s41467-023-38000-y](https://doi.org/10.1038/s41467-023-38000-y).
- [24] Pengfei Xie, Yonggang Yao, Zhennan Huang, Zhenyu Liu, Junlei Zhang, Tangyuan Li, Guofeng Wang, Reza Shahbazian-Yassar, Liangbing Hu, and Chao Wang, “Highly efficient decomposition of ammonia using high-entropy alloy catalysts”, *Nature Communications* (5, 2019), DOI: [10.1038/s41467-019-11848-9](https://doi.org/10.1038/s41467-019-11848-9).
- [25] Yao Qiu, Sebastian Thomas, Mark A. Gibson, Hamish L. Fraser, and Nick Birbilis, “Corrosion of high entropy alloys”, *npj Materials Degradation* (21, 2017), DOI: [10.1038/s41529-017-0009-y](https://doi.org/10.1038/s41529-017-0009-y).
- [26] Yusi Xie, Dorota M. Artymowicz, Pietro P. Lopes, Ashlee Aiello, Duo Wang, James L. Hart, Elaf Anber, Mitra L. Taheri, Houlong Zhuang, Roger C. Newman, and Karl Sieradzki, “A percolation theory for designing corrosion-resistant alloys”, *Nature Materials* (2021), DOI: [10.1038/s41563-021-00920-9](https://doi.org/10.1038/s41563-021-00920-9).
- [27] W. H. Blades, B. W. Y. Redemann, N. Smith, D. Sur, M. S. Barbieri, Y. Xie, S. Lech, E. Anber, M. L. Taheri, C. Wolverton, T. M. McQueen, J. R. Scully, and K. Sieradzki, “Tuning chemical short-range order for stainless behavior at reduced chromium concentrations in multi-principal element alloys”, *Acta Materialia* (15, 2024), DOI: [10.1016/j.actamat.2024.120209](https://doi.org/10.1016/j.actamat.2024.120209).
- [28] Easo P. George, Dierk Raabe, and Robert O. Ritchie, “High-entropy alloys”, *Nature Reviews Materials* (2019), DOI: [10.1038/s41578-019-0121-4](https://doi.org/10.1038/s41578-019-0121-4).
- [29] Sheng Yin, Yunxing Zuo, Anas Abu-Odeh, Hui Zheng, Xiang-Guo Li, Jun Ding, Shyue Ping Ong, Mark Asta, and Robert O. Ritchie, “Atomistic simulations of dislocation mobility in refractory high-entropy alloys and the effect of chemical short-range order”, *Nature Communications* (11, 2021), DOI: [10.1038/s41467-021-25134-0](https://doi.org/10.1038/s41467-021-25134-0).
- [30] Daniel Utt, Subin Lee, Yaolong Xing, Hyejin Jeong, Alexander Stukowski, Sang Ho Oh, Gerhard Dehm, and Karsten Albe, “The origin of jerky dislocation motion in high-entropy alloys”, *Nature Communications* (15, 2022), DOI: [10.1038/s41467-022-32134-1](https://doi.org/10.1038/s41467-022-32134-1).
- [31] X. Zhou, J. R. Mianroodi, A. Kwiatkowski da Silva, T. Koenig, G. B. Thompson, P. Shanthraj, D. Ponge, B. Gault, B. Svendsen, and D. Raabe, “The hidden structure dependence of the chemical life of dislocations”, *Science Advances* (16, 2021), DOI: [10.1126/sciadv.abf0563](https://doi.org/10.1126/sciadv.abf0563).
- [32] Saman Moniri, Yao Yang, Jun Ding, Yakun Yuan, Jihan Zhou, Long Yang, Fan Zhu, Yuxuan Liao, Yonggang Yao, Liangbing Hu, Peter Ercius, and Jianwei Miao, “Three-dimensional atomic structure and local chemical order of medium- and high-entropy nanoalloys”, *Nature* (2023), DOI: [10.1038/s41586-023-06785-z](https://doi.org/10.1038/s41586-023-06785-z).
- [33] Xuefei Chen, Qi Wang, Zhiying Cheng, Mingliu Zhu, Hao Zhou, Ping Jiang, Lingling Zhou, Qiqi Xue, Fuping Yuan, Jing Zhu, Xiaolei Wu, and En Ma, “Direct observation of chemical short-range order in a medium-entropy alloy”, *Nature* (2021), DOI: [10.1038/s41586-021-03428-z](https://doi.org/10.1038/s41586-021-03428-z).
- [34] Ruopeng Zhang, Shiteng Zhao, Jun Ding, Yan Chong, Tao Jia, Colin Ophus, Mark Asta, Robert O. Ritchie, and Andrew M. Minor, “Short-range order and its impact on the CrCoNi medium-entropy alloy”, *Nature* (2020), DOI: [10.1038/s41586-020-2275-z](https://doi.org/10.1038/s41586-020-2275-z).
- [35] Scott Atchley, Christopher Zimmer, John Lange, David Bernholdt, Veronica Melesse Vergara, Thomas Beck, Michael Brim, Reuben Budiardja, Sunita Chandrasekaran, Markus Eisenbach, Thomas Evans, Matthew Ezell, Nicholas Frontiere, Antigoni Georgiadou, Joe Glenski, Philipp Grete, Steven Hamilton, John Holmen, Axel Huebl, Daniel Jacobson, Wayne Joubert, Kim McMahon, Elia Merzari, Stan Moore, Andrew Myers, Stephen Nichols, Sarp Oral, Thomas Papatheodore, Danny Perez, David M. Rogers, Evan Schneider, Jean-Luc Vay, and P. K. Yeung, “Frontier: Exploring Exascale”, *Proceedings of the International Conference for High Performance Computing, Networking, Storage and Analysis, SC '23*, Association for Computing Machinery, 11, 2023, DOI: [10.1145/3581784.3607089](https://doi.org/10.1145/3581784.3607089).
- [36] Yifan Cao, Killian Sheriff, and Rodrigo Freitas, *Capturing short-range order in high-entropy alloys with machine learning potentials*, 2024, arXiv: [2401.06622](https://arxiv.org/abs/2401.06622) cond-mat.mtrl-sci, URL: <https://arxiv.org/abs/2401.06622>.
- [37] Nikolay Zotov, Konstantin Gubaev, Julian Wörner, and Blazej Grabowski, “Moment tensor potential for static and dynamic investigations of screw dislocations in bcc Nb”, *Modelling and Simulation in Materials Science and Engineering* (1, 2024), DOI: [10.1088/1361-651X/ad2d68](https://doi.org/10.1088/1361-651X/ad2d68).
- [38] Rui Wang, Lingyu Zhu, Subrahmanyam Pattamatta, David J. Srolovitz, and Zhaoxuan Wu, *The Taming of the Screw: Dislocation Cores in BCC Metals and Alloys*, 21, 2022, DOI: [10.48550/arXiv.2209.12323](https://doi.org/10.48550/arXiv.2209.12323).
- [39] John Price Hirth, Jens Lothe, and Toshio Mura, “Theory of dislocations”, *Journal of Applied Mechanics* (1983).
- [40] Vaclav Vitek, “Intrinsic stacking faults in body-centred cubic crystals”, *Philosophical Magazine* (1968).
- [41] Rodrigo Freitas and Yifan Cao, “Machine-learning potentials for crystal defects”, *MRS Communications* (1, 2022), DOI: [10.1557/s43579-022-00221-5](https://doi.org/10.1557/s43579-022-00221-5).
- [42] Sheng Yin, Jun Ding, Mark Asta, and Robert O. Ritchie, “Ab initio modeling of the energy landscape for screw dislocations in body-centered cubic high-entropy alloys”, *npj Computational Materials* (29, 2020), DOI: [10.1038/s41524-020-00377-5](https://doi.org/10.1038/s41524-020-00377-5).
- [43] Chanhoo Lee, Francesco Maresca, Rui Feng, Yi Chou, T. Ungar, Michael Widom, Ke An, Jonathan D. Poplawsky, Yi-Chia Chou, Peter K. Liaw, and W. A. Curtin, “Strength can be controlled by edge dislocations in refractory high-entropy alloys”, *Nature Communications* (16, 2021), DOI: [10.1038/s41467-021-25807-w](https://doi.org/10.1038/s41467-021-25807-w).
- [44] Killian Sheriff, Daniel Xiao, Yifan Cao, Lewis R. Owen, and Rodrigo Freitas, *Machine learning potentials for modeling alloys across compositions*, 14, 2025, DOI: [10.48550/arXiv.2506.12592](https://doi.org/10.48550/arXiv.2506.12592).
- [45] John P. Perdew, Kieron Burke, and Matthias Ernzerhof, “Generalized Gradient Approximation Made Simple”, *Phys. Rev. Lett.* (18 1996), DOI: [10.1103/PhysRevLett.77.3865](https://doi.org/10.1103/PhysRevLett.77.3865).
- [46] P. E. Blöchl, “Projector augmented-wave method”, *Phys. Rev. B* (24 1994), DOI: [10.1103/PhysRevB.50.17953](https://doi.org/10.1103/PhysRevB.50.17953).
- [47] Georg Kresse and Jürgen Hafner, “Ab initio molecular dynamics for liquid metals”, *Physical Review B* (1993), DOI: [10.1103/PhysRevB.47.558](https://doi.org/10.1103/PhysRevB.47.558).

- [48] Georg Kresse and Jürgen Furthmüller, “Efficient iterative schemes for ab initio total-energy calculations using a plane-wave basis set”, *Physical Review B* (1996), DOI: [10.1103/PhysRevB.54.11169](https://doi.org/10.1103/PhysRevB.54.11169).
- [49] Georg Kresse and Jürgen Furthmüller, “Efficiency of ab-initio total energy calculations for metals and semiconductors using a plane-wave basis set”, *Computational Materials Science* (1996), DOI: [10.1016/0927-0256\(96\)00008-0](https://doi.org/10.1016/0927-0256(96)00008-0).
- [50] Georg Kresse and Jürgen Hafner, “Ab initio molecular-dynamics simulation of the liquid-metal-amorphous-semiconductor transition in germanium”, *Physical Review B* (1994), DOI: [10.1103/PhysRevB.49.14251](https://doi.org/10.1103/PhysRevB.49.14251).
- [51] Georg Kresse and Daniel Joubert, “From ultrasoft pseudopotentials to the projector augmented-wave method”, *Physical Review B* (1999), DOI: [10.1103/PhysRevB.59.1758](https://doi.org/10.1103/PhysRevB.59.1758).
- [52] Ralf Drautz, “Atomic cluster expansion for accurate and transferable interatomic potentials”, *Physical Review B* (8, 2019), DOI: [10.1103/PhysRevB.99.014104](https://doi.org/10.1103/PhysRevB.99.014104).
- [53] Yury Lysogorskiy, Cas van der Oord, Anton Bochkarev, Sarath Menon, Matteo Rinaldi, Thomas Hammerschmidt, Matous Mrovec, Aidan Thompson, Gábor Csányi, Christoph Ortner, and Ralf Drautz, “Performant implementation of the atomic cluster expansion (PACE) and application to copper and silicon”, *npj Computational Materials* (28, 2021), Publisher: Nature Publishing Group, DOI: [10.1038/s41524-021-00559-9](https://doi.org/10.1038/s41524-021-00559-9).
- [54] Aidan P. Thompson, H. Metin Aktulga, Richard Berger, Dan S. Bolintineanu, W. Michael Brown, Paul S. Crozier, Pieter J. in ’t Veld, Axel Kohlmeyer, Stan G. Moore, Trung Dac Nguyen, Ray Shan, Mark J. Stevens, Julien Tranchida, Christian Trott, and Steven J. Plimpton, “LAMMPS - a flexible simulation tool for particle-based materials modeling at the atomic, meso, and continuum scales”, *Computer Physics Communications* (1, 2022), DOI: [10.1016/j.cpc.2021.108171](https://doi.org/10.1016/j.cpc.2021.108171).
- [55] Luis A. Zepeda-Ruiz, Alexander Stukowski, Tomas Opperstrup, Nicolas Bertin, Nathan R. Barton, Rodrigo Freitas, and Vasily V. Bulatov, “Atomistic insights into metal hardening”, *Nature Materials* (2021), DOI: [10.1038/s41563-020-00815-1](https://doi.org/10.1038/s41563-020-00815-1).
- [56] Luis A. Zepeda-Ruiz, Alexander Stukowski, Tomas Opperstrup, and Vasily V. Bulatov, “Probing the limits of metal plasticity with molecular dynamics simulations”, *Nature* (2017), DOI: [10.1038/nature23472](https://doi.org/10.1038/nature23472).
- [57] Alexander Stukowski and Karsten Albe, “Extracting dislocations and non-dislocation crystal defects from atomistic simulation data”, *Modelling and Simulation in Materials Science and Engineering* (2010), ISSN: 0965-0393, DOI: [10.1088/0965-0393/18/8/085001](https://doi.org/10.1088/0965-0393/18/8/085001).
- [58] Tim Hsu, Babak Sadigh, Nicolas Bertin, Cheol Woo Park, James Chapman, Vasily Bulatov, and Fei Zhou, “Score-based denoising for atomic structure identification”, *npj Computational Materials* (18, 2024), DOI: [10.1038/s41524-024-01337-z](https://doi.org/10.1038/s41524-024-01337-z).
- [59] Alexander Stukowski, “Visualization and analysis of atomistic simulation data with OVITO—the Open Visualization Tool”, *Modelling and Simulation in Materials Science and Engineering* (2009), ISSN: 0965-0393, DOI: [10.1088/0965-0393/18/1/015012](https://doi.org/10.1088/0965-0393/18/1/015012).
- [60] Nicholas Metropolis, Arianna W. Rosenbluth, Marshall N. Rosenbluth, Augusta H. Teller, and Edward Teller, “Equation of State Calculations by Fast Computing Machines”, *The Journal of Chemical Physics* (1, 1953), DOI: [10.1063/1.1699114](https://doi.org/10.1063/1.1699114).
- [61] W. K. Hastings, “Monte Carlo Sampling Methods Using Markov Chains and Their Applications”, *Biometrika* (1970), DOI: [10.2307/2334940](https://doi.org/10.2307/2334940).
- [62] Tess E. Smidt, “Euclidean Symmetry and Equivariance in Machine Learning”, *Trends in Chemistry* (1, 2021), ISSN: 2589-7209, 2589-5974, DOI: [10.1016/j.trechm.2020.10.006](https://doi.org/10.1016/j.trechm.2020.10.006).
- [63] David JC MacKay, *Information theory, inference and learning algorithms*, Cambridge university press, 2003.
- [64] J. M. Cowley, “An Approximate Theory of Order in Alloys”, *Physical Review* (1, 1950), DOI: [10.1103/PhysRev.77.669](https://doi.org/10.1103/PhysRev.77.669).
- [65] R. M. J. Cotterill, “Does dislocation density have a natural limit?”, *Physics Letters A* (24, 1977), DOI: [10.1016/0375-9601\(77\)90321-8](https://doi.org/10.1016/0375-9601(77)90321-8).
- [66] Ying Han, Hangman Chen, Yongwen Sun, Jian Liu, Shaolou Wei, Bijun Xie, Zhiyu Zhang, Yingxin Zhu, Meng Li, Judith Yang, Wen Chen, Penghui Cao, and Yang Yang, “Ubiquitous short-range order in multi-principal element alloys”, *Nature Communications* (1, 2024), DOI: [10.1038/s41467-024-49606-1](https://doi.org/10.1038/s41467-024-49606-1).
- [67] Xinran Zhou, Sicong He, and Jaime Marian, “Cross-kinks control screw dislocation strength in equiatomic bcc refractory alloys”, *Acta Materialia* (1, 2021), DOI: [10.1016/j.actamat.2021.116875](https://doi.org/10.1016/j.actamat.2021.116875).
- [68] Gaia Righi, Carlos J. Ruestes, Camelia V. Stan, Suzanne J. Ali, Robert E. Rudd, Megumi Kawasaki, Hye-Sook Park, and Marc A. Meyers, “Towards the ultimate strength of iron: spalling through laser shock”, *Acta Materialia* (15, 2021), DOI: [10.1016/j.actamat.2021.117072](https://doi.org/10.1016/j.actamat.2021.117072).
- [69] Qi Tang and Mostafa Hassani, “Quantifying dislocation drag at high strain rates with laser-induced Microprojectile impact”, *International Journal of Plasticity* (1, 2024), DOI: [10.1016/j.ijplas.2024.103924](https://doi.org/10.1016/j.ijplas.2024.103924).
- [70] N. T. Switzner, C. J. Van Tyne, and M. C. Mataya, “Effect of forging strain rate and deformation temperature on the mechanical properties of warm-worked 304L stainless steel”, *Journal of Materials Processing Technology* (1, 2010), DOI: [10.1016/j.jmatprotec.2010.01.014](https://doi.org/10.1016/j.jmatprotec.2010.01.014).
- [71] Peter U. Nwachukwu and Oluleke O. Oluwole, “Effects of rolling process parameters on the mechanical properties of hot-rolled St60Mn steel”, *Case Studies in Construction Materials* (1, 2017), DOI: [10.1016/j.cscm.2017.01.006](https://doi.org/10.1016/j.cscm.2017.01.006).
- [72] S. P. F. C. Jaspers and J. H. Dautzenberg, “Material behaviour in metal cutting: strains, strain rates and temperatures in chip formation”, *Journal of Materials Processing Technology* (14, 2002), DOI: [10.1016/S0924-0136\(01\)01227-4](https://doi.org/10.1016/S0924-0136(01)01227-4).
- [73] Keguo Zhang, Keyi Wang, Zhanqiang Liu, and Xiaodong Xu, “Strain Rate of Metal Deformation in the Machining Process from a Fluid Flow Perspective”, *Applied Sciences* (2020), DOI: [10.3390/app10093057](https://doi.org/10.3390/app10093057).

- [74] Biao Xu, Shihua Ma, Shasha Huang, Jun Zhang, Yaoxu Xiong, Haijun Fu, Xuepeng Xiang, and Shijun Zhao, “Influence of short-range order on diffusion in multiprincipal element alloys from long-time atomistic simulations”, *Physical Review Materials* (30, 2023), DOI: [10 . 1103 / PhysRevMaterials.7.033605](https://doi.org/10.1103/PhysRevMaterials.7.033605).
- [75] Killian Sheriff, Yifan Cao, and Rodrigo Freitas, URL: [https : / / github . com / killiansheriff / ChemicalMotifIdentifier](https://github.com/killiansheriff/ChemicalMotifIdentifier).
- [76] Killian Sheriff and Rodrigo Freitas, URL: <https://github.com/killiansheriff/Machine-learning-potentials-for-modeling-alloys-across-compositions>.
- [77] Killian Sheriff, *LovelyPlots: A collection of matplotlib stylesheets for scientific figures*, 2023, DOI: [10 . 5281 / zenodo.6903936](https://doi.org/10.5281/zenodo.6903936).